

Support dependence of MeOH decomposition over size-selected Pt nanoparticles

Jason R. Croy¹, S. Mostafa¹, J. Liu², Yongho Sohn², H. Heinrich^{1,2}, B. Roldan Cuenya¹

¹Department of Physics, University of Central Florida, Orlando FL 32816

²Center of Advanced Materials Processing and Characterization, University of Central Florida, Orlando, FL 32816

Abstract

We present here the decomposition of methanol over Pt nanoparticles supported on a series of oxide powders. The samples tested may be roughly grouped in two categories consisting of large (~ 15-18 nm) and small (~ 8-9 nm) Pt particles deposited on *reducible* (CeO₂, TiO₂) and *non-reducible* (SiO₂, ZrO₂, Al₂O₃) supports. The smallest particles (~ 8 nm), deposited on ZrO₂, were found to be cationic and the most active for the decomposition of methanol. Furthermore, the stability of metallic Pt and its oxides was observed to be dependent on the choice of support. In all Pt containing samples the reaction proceeds via the direct decomposition of methanol, as no significant amounts of by-products were detected in the experimental range of 100 - 300°C.

1. Introduction

Methanol (MeOH) as a chemical commodity has become a staple of the modern world. Consequently, the synthesis of MeOH has long been an important topic and there is today a preferred catalytic system in wide-spread industrial use (Cu/ZnO/Al₂O₃) [1]. In the reverse direction, the decomposition of MeOH has increased in significance due to its applicability as a storage fuel for hydrogen and subsequent use in fuel cells. In addition, methanol's adaptability to the existing infrastructure (i.e. as a liquid fuel) makes the direct methanol fuel cell (DMFC) an attractive technology for transportation applications [2]. There are several decomposition processes currently in use and under

study including direct decomposition, steam reforming, and oxidation [3]. These processes require the use of metallic nanoparticle catalysts such as Cu, Pt, and Pd supported on various oxides [4]. However, because a fundamental knowledge of these processes is still lacking, MeOH decomposition and combustion are still subjects of intense studies [5], as is the interaction of MeOH with surfaces relevant to electro-oxidation for fuel cell technologies [6-10].

There is a current debate in the literature on whether metallic Pt or Pt oxides are the most catalytically active species. As an example, PtO₂(110) surfaces have been found more reactive than metallic Pt for CO oxidation [11]. Dam al. [12] have shown that Pt dissolution in fuel cells reaches a saturation level due to the presence of a protective platinum oxide layer, and Hull et al. [13] showed enhanced activity for Pt-carbon nanotube catalysts, where the Pt particles are covered by a thin PtO_x shell. On the other hand, the temporal decay in the performance of Pt-based fuel cell electrodes has been attributed to the formation of PtO and Pt dissolution [14].

In a previous work [15], we have shown that Pt nanoparticles supported on anatase TiO₂ have a size-dependent activity in the decomposition of MeOH, where an increase in activity was associated with a decrease in particle size. Furthermore, the oxidation state of the nanoparticles depended on the initial size of the particles. Although support related effects were not considered, owing to the use of a common support, they were assumed to be present and are in need of consideration. For example, reactive sites are expected to be present at the nanoparticle's perimeter associated with atoms in contact with the support [16,17] and at the support itself [18,19]. Metal-support interactions are also responsible for varying degrees of encapsulation of metallic particles in several oxide systems [20-24], and it has been shown that the acidity of the support

plays a major role in the electronic state of the supported particles and thus can influence catalytic performance [25].

Although the smallest particles in the current study are relatively large (~ 8 nm), it will be shown that metal-support interactions are still important, especially in connection with particle oxidation state and stability against coarsening.

2. Experimental

Non-polar/polar diblock copolymers [Poly(styrene)-block-poly(2vinylpyridine), Polymer Source Inc.] were dissolved in a non-polar solvent (toluene) in order to obtain spherical nano-cages (inverse micelles). These micelles were then loaded with a metal salt ($\text{H}_2\text{PtCl}_6 \cdot 6\text{H}_2\text{O}$) to produce self-confined and size-selected Pt nanoparticles. The particle size was controlled by using a polymer with a specific head length [PS(27700)-PVP(4300), i.e. constant PVP molecular weight for all samples] and by tuning the metal-salt/polymer head concentration in the solution [26-28]. The solution was then mixed with a series of oxides [TiO_2 (anatase), CeO_2 , ZrO_2 , $\alpha\text{-Al}_2\text{O}_3$, and SiO_2] in the form of a powder having nominal grain sizes of in the range of 32 nm to 45 nm,. All samples were calcined in air at 500°C for 2.5 hours. Each catalyst sample had a total weight of 100 mg and contained 2% by weight Pt. A metal-salt/PVP concentration ratio of 0.6 was used to create Pt nanoparticles having a narrow size distribution. The one exception was a second Pt/ CeO_2 sample prepared with the same polymer, but with a metal-salt/PVP concentration of 0.2, Figure 1. This resulted in a solution of Pt particles with a smaller average size, labeled Pt/ CeO_2 (#2). A second solution was desirable in the case of CeO_2 -supported particles since significant nanoparticle sintering was observed in this support upon our thermal treatment.

Powder samples were deposited on carbon-coated stickers and transferred to an ultra high vacuum system (UHV, SPECS GmbH) for surface analysis by X-ray photoelectron spectroscopy (XPS). XPS data were collected using a monochromatic X-ray source (Al-K α , 1486.6 eV) operating at 300 W and a flood gun was used to correct for surface charging during measurement. The respective binding energies of the powder samples were referenced to the Ti 2p_{3/2} [TiO₂] peak at 458.6 eV [29], Ce 3d_{5/2} [CeO₂] at 882.2 eV [30], Al 2p_{3/2} [Al₂O₃] at 74.5 eV [31], Si 2p_{3/2} [SiO₂] at 103.8 eV [32], and Zr 3d_{3/2} [ZrO₂] at 183.0 eV [33].

Catalytic decomposition of methanol in the vapor phase was carried out in a packed-bed mass flow reactor with a vertical quartz tube (inside diameter 4 mm) serving as the reactor vessel. In order to promote flow through the reactor, the powder catalysts (100 mg, 2% wt Pt) were mixed with 200 mg of inert quartz sand and divided into six 50 mg segments. These segments were separated and supported in the reactor by glass wool plugs. A thermocouple (K-type) in contact with the reactor was used to monitor temperature. Immediately prior to the reaction all catalysts were heated for one hour at ~200°C (below the initial calcination temperatures used to remove the polymeric nanoparticle shell) in a flow of He at 10 ml/min. Activities were measured at atmospheric pressure in the range of 100 to 300 °C. Helium was used as the carrier gas during all reactions and regulated at 10 ml/min by a mass flow controller (MKS). The product stream of the reactor was monitored by a quadrupole mass spectrometer (QMS, HIDEN, HPR-20) with partial pressures of the product gases measured using the system's Faraday cup and SEM detectors. The QMS inlet has a maximum consumption of 16 ml/min and several flow experiments were conducted to optimize the experimental conditions. The composition of the feed was 0.01% MeOH relative to the flow of He, as determined by the partial pressures of He and the main fragment ion of MeOH (m/q = 31).

The polymer-salt solutions were also dip-coated on SiO₂/Si(001) substrates in order to obtain particle size information (height) via atomic force microscopy (AFM) with a Nanoscope Multimode (Digital Instruments) microscope operating in tapping mode. In addition, transmission electron microscopy (TEM) was carried out on the powder samples with a Tecnai F30 TEM operating at an accelerating voltage of 300 kV.

3. Results and discussion

3.1 Morphological and structural characterization

Fig. 1 displays AFM images of the nanoparticle polymeric solutions dip-coated on SiO₂/Si(001) after UHV annealing for 30 min at 500°C. Fig. 1(a) shows the particle solution used in all samples except the Pt/CeO₂(#2) which is shown in Fig 1(b). At this temperature, removal of the encapsulating polymer is observed by monitoring the C-1s XPS signal. Analysis of the images taken after annealing gives average particle height distributions of 5.1 ± 0.6 nm for (a), and 2.7 ± 0.5 for (b).

Figures 2(b-d) and 3 show typical bright-field TEM images of Pt nanoparticles supported on selected oxide powders. All samples underwent the same thermal treatments as described above and were prepared using the same nanoparticle polymeric solution [except Pt/CeO₂(#2)]. Low magnification images were employed to obtain the average diameter of the Pt nanoparticles supported on the oxide powders.

Fig. 2(a) displays a high angle annular dark field image, obtained by scanning transmission electron microscopy (STEM), of the Pt/CeO₂(#1) sample. The light-colored areas in this image correspond to Pt-rich regions. Fig. 2(b) shows a bright field image of the same region, and (c) shows a high resolution image of a Pt particle (~ 14 nm) [marked by (1) in Fig. 2(b)] in this sample. From Fig. 2(c) a lattice parameter of 3.95 ± 0.04 Å was obtained, in good agreement with literature values of 3.92 Å for fcc-Pt [34]. In Fig.

2(c) the nanoparticle appears faceted (typical feature of nanoparticles in this sample) and a Pt(111) terrace is observed. For this sample, the support itself (CeO_2) displays significant agglomeration after annealing in air. In addition, the average Pt particle size in this sample was 14.6 ± 2.7 nm, indicating that strong nanoparticle coarsening had occurred. One explanation for sintering could be, as given by Perrichon et al. [35], the destabilization of Pt particles on ceria. This effect stems from surface reorganization induced by O^{2-} mobility at temperatures near 300°C , which is below our calcination temperature (500°C). The authors also show an encapsulation/decoration effect which increases with increasing reduction temperatures with smaller particles being more susceptible to this phenomenon. This possibility will be discussed in connection with the activity of our two Pt/ CeO_2 samples. Fig. 2(d) shows a Pt particle (~ 12 nm) in our sample labeled Pt/ CeO_2 (#2). This sample was made from a particle solution having a size distribution roughly half the size of the Pt/ CeO_2 (#1) sample. Analysis of the HRTEM image of a small Pt particle in this sample indicated a slightly higher value for the lattice parameter (4.0 ± 0.04). Penner et al. [36] have observed the formation of Pt-ceria alloys starting at $\sim 450^\circ\text{C}$ with a lattice parameter of 4.16 \AA . Because this sample underwent the same thermal treatment as the Pt/ CeO_2 (#1) sample, and both samples show similar activities and size distributions, we might conclude that Pt particles, supported on CeO_2 , are not stable at annealing temperatures of 500°C or more, and Pt ceria alloys can be formed. In particular, smaller Pt particles seem to be more susceptible to the interaction with CeO_2 , in agreement with Perrichon et al. [35]. On Ce thin films deposited on Pt foils, Tang et al. [37] found evidence of strong Ce-Pt interactions and interdiffusion (rather than encapsulation) at and above room temperature. The presence of Pt-oxides at the nanoparticle's surface could not be detected by TEM, but will be discussed in the next section based on our XPS data.

For the Pt/SiO₂ sample, Fig 3(a), a similar sintering behavior was observed. However, in this sample the distribution of particle sizes was very broad and averaged 15 ± 10 nm. This might be related to the fact that the support itself was not of nanometer scale, but rather started out as large (1/8") pellets and was ground by hand into agglomerated powder. This may present to the supported particles a more widely distributed set of surface sites available for nucleation as compared to the already nanometer-sized ceria support. However, sintering of Pt on SiO₂ is not a new phenomenon and can be more prominent when heating takes place in air as compared to an inert atmosphere [38]. Fig. 3(a)(insert) displays a uniform region within the Pt/SiO₂ sample.

The Pt/Al₂O₃, Fig 3(b), and Pt/ZrO₂, Fig. 3(c),(d), each show similar size distributions with diameters of 8.7 ± 2.1 nm and 8.3 ± 1.6 nm, respectively. These values are also in close proximity to the distribution of the Pt/TiO₂ sample having an average particle diameter of 8.6 ± 1.2 nm, details and images of which can be found in Ref. [15].

3.2 *Electronic and chemical characterization*

Fig. 4 shows XPS spectra of Pt deposited on the different oxide powder supports measured after annealing at 500°C. In Fig. 4(a) the solid lines indicate the positions of the main core-level peaks of metallic Pt at 71.1 eV (4f_{7/2}) and 74.3 eV (4f_{5/2}), the dashed lines Pt²⁺ in PtO (73.3 and 76.6 eV), and the dotted lines Pt⁴⁺ in PtO₂ (75.0 and 78.8 eV). For the Pt/TiO₂ sample, we see that it is predominantly metallic with the 4f_{7/2} appearing at ~ 70.5 eV. This corresponds to a negative binding energy shift of ~ 0.6 eV with respect to the bulk value of 71.1 eV. This is in agreement with our previous results [15] and is close to values reported elsewhere for similar TiO₂-supported Pt particles [39]. Such negative energy shifts can be explained by charge transfer to the particle from the support due to delocalized electron distributions arising from oxygen vacancies [40], or

small particles with a large number of surface atoms having reduced coordination numbers [41]. The Pt/ZrO₂ and Pt/SiO₂ show a convolution of Pt²⁺ and Pt⁴⁺, with the former being mainly Pt²⁺ and the latter slightly favoring contributions from Pt⁴⁺. The Pt/CeO₂(#1) sample appears highly oxidized (mainly Pt⁴⁺) and the higher binding energies indicate a strong interaction between the CeO₂ support and the Pt particles. As was mentioned before, the possible formation of Pt-Ce alloys might explain the anomalously large binding energies observed in the XPS data of these samples. For the Pt/CeO₂(#2) sample, a similar spectrum was obtained as that shown for the Pt/CeO₂(#1) sample. Tang et al. have shown shifts to higher binding energies (+0.2 eV with respect to bulk Pt) for ultrathin Ce films deposited on a metallic Pt foil [37]. In this work, the authors highlight the formation of Ce/Pt mixed layers due to enhanced interdiffusion at and above RT. In the case of our supported Pt nanoparticles, the large BE shifts observed for the Pt-4f core levels can be attributed to Pt^{δ+} species alloyed with cerium atoms upon annealing at 500°C. Simply based on our XPS data (averaged from the sampling depth, where a Ce concentration gradient exists) we cannot conclude whether Ce atoms are at the surface of the Pt clusters (encapsulation effects) or they are surrounded by Pt atoms in intermetallic compounds. A previous work by Fu et al. [42] also discusses the possibility of Pt ion diffusion into subsurface CeO₂ layers. Interestingly, and in agreement with our results, their XPS spectra obtained on 2.5 nm-large Pt nanoparticles supported on CeO₂ (6 nm) after calcination at 500°C indicate the presence of Pt-oxide species, mainly Pt⁴⁺.

Fig. 4(b) shows the Pt 4d_{5/2} peak in the Pt/Al₂O₃ sample appearing at ~ 314.0 eV for Pt⁰ (solid line) and ~ 317.5 eV for Pt²⁺ (dashed line). Here again, as in the case of Pt/TiO₂, this sample is mainly Pt⁰ and shows a negative binding energy shift of ~ 0.6 eV as compared to the bulk value of metallic Pt at 314.6 eV. Fig 4(c) shows the Pt 4f region for the Pt/Al₂O₃ sample. Here the Al 2p_{3/2} at 74.5 eV falls in the middle of the range

where we expect to see the Pt 4f peaks. Shown is a superposition of two spectra taken before and after the addition of Pt to our Al₂O₃ support. The shoulder, due to Pt, is emphasized with an arrow and the difference between the two curves (Pt contribution) is plotted at the bottom of the graph.

3.2 Catalytic activity and selectivity

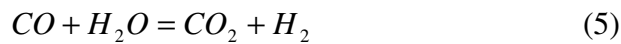
Fig. 5 displays the activity and selectivity for the decomposition of MeOH of the different oxide powders prior to the addition of Pt. Activity is defined in terms of MeOH conversion and is given by the equation

$$\frac{P_i - P_T}{P_i} \times 100 \quad (1)$$

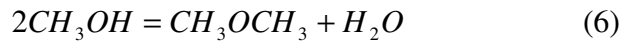
Where P_i is the initial partial pressure of the main fragment ion of methanol ($m/q = 31$) and P_T is the partial pressure at a given temperature throughout the experiment. The percentages along the top of each graph represent the MeOH conversion at a particular temperature as given by equation (1). Selectivity for each product gas is derived from the QMS data, along with stoichiometric considerations [equations (3)-(5)], and is defined as the percent of the total product that each particular partial gas pressure represents,

$$selectivity (\%) = \frac{A_n}{\sum A_n} \times 100 \quad (2)$$

Where A_n represents the output of the n^{th} product gas. In our experiments CO₂, and Dimethyl ether (DME) were obtained as by-products. CO₂ originates from CO produced in the decomposition of MeOH, reaction (3), and possible mechanisms involved in the production of CO₂ are the Boudouard and water gas shift reactions, (4) and (5) respectively:



DME may be formed according to equation (6).



We note that during the catalyst's time on-line (~ 7 hours) we do not observe any deactivation or visible change in the catalyst and we might then rule out reaction (4) as giving a significant contribution. However, long-term deactivation studies have not yet been performed on these catalysts.

The SiO₂ support is absent in Fig. 5 because it was found to be inert over the range of temperatures used in the experiment (100°C to 300°C). The TiO₂ (a) and the Al₂O₃ (d) each show similar selectivity with a tendency towards the formation of DME. However, the selectivity of DME for the Al₂O₃ remains high even at 300°C, whereas the TiO₂ shows a marked switch towards H₂ at that temperature. The ZrO₂ sample (c) remains inactive at temperatures below 200°C and no by-products are detected up to 300°C. For the CeO₂ sample (b), which becomes active at temperatures above 150°C, we see a high selectivity for H₂ and ~ 6% for CO₂ at 250°C decreasing to ~ 2 % by 300°C. The formation of CO₂ could favor catalyst lifetime since CO poisoning will be reduced. From the QMS data, equations (3) and (5), and neglecting (4), it was estimated that ~ 20 % of the CO from MeOH decomposition goes to CO₂ through the shift reaction at 250°C. This sample also shows excellent activity relative to the other supports with almost 100 % conversion at 300°C. TiO₂ being the second most active with only 54 % conversion at 300°C. None of the supports tested were active for MeOH decomposition at or below 150°C.

Fig. 6 shows the same type of data for the supports after the addition of Pt nanoparticles. Here we show a plot of MeOH conversion (%) as a function of the reactor temperature with the dotted line denoting 50 % conversion. In all of the Pt containing samples no by-products were observed in the range of temperatures tested. Therefore, the reaction proceeds by way of direct decomposition. Again, as in Fig. 5, we see similarities between the Pt/TiO₂ and Pt/Al₂O₃ samples. Pt/TiO₂ and Pt/Al₂O₃ have similar average particle size distributions of ~ 8.6 - 8.7 nm, and show similar activity. The Pt/Al₂O₃ slightly outperforms the Pt/TiO₂ sample reaching a higher conversion at 250°C. For the Pt/ZrO₂ sample (Pt diameter ~ 8.3 ± 1.6 nm) we see that it is by far the most active at low temperatures reaching 73 % conversion at 200°C. The Pt/SiO₂ (Pt diameter ~ 15.0 ± 10.4 nm) now becomes active above 150°C with excellent selectivity for H₂ and ~ 60 % conversion at 300°C. Because the SiO₂ support was completely inactive we may attribute this activity to the addition of Pt. Although the average Pt particle size in the Pt/CeO₂(#1) sample is much larger than that on the other substrates (~14.6 ± 2.7 nm) its activity is only slightly lower than that of Pt/TiO₂ and Pt/Al₂O₃. This effect may be attributed to the relatively high MeOH conversion observed on our Pt-free nanocrystalline CeO₂ powders, and the addition of even large Pt particles further enhanced the activity. Because this support performed relatively well before the addition of Pt, and our TEM images show agglomeration on this sample [Fig. 2(a),(b)], an additional sample was prepared with the goal of minimizing particle growth. This was done by preparing an alternate micelle solution with a Pt particle size distribution roughly half the size of the initial sample, as seen in the AFM images of Fig. 1. From here the same thermal treatment was done as on the initial sample and TEM images were taken. Unfortunately the new sample, denoted as Pt/CeO₂(#2), produced analogous reactivity results, also shown in Fig 6. The TEM images obtained from this sample, after annealing

in air at 500°C and before the reaction, were very similar to those of the first Pt/CeO₂(#1) sample (Fig. 2) revealing considerable particle sintering.

The general order for reaching the 50% conversion mark may be listed as follows: Pt/ZrO₂, Pt/Al₂O₃, Pt/TiO₂, Pt/CeO₂, Pt/SiO₂. Surprisingly, this trend does not seem to correlate with the enhanced catalytic activity expected for nanoparticles supported on highly reducible oxides. However, it is in agreement with Ref. [43] and results obtained by Usami et. al. [44] who have shown that Pd/ZrO₂ is more active for MeOH decomposition than Pd/CeO₂, Pd/TiO₂, as well as Pd/SiO₂. In addition, the authors determined that cationic Pd was advantageous for this reaction, in agreement with the XPS data (Fig. 4) of our Pt/ZrO₂ sample.

An important point to note is that the least active samples (Pt/CeO₂ and Pt/SiO₂) both show particle coarsening with a significant increase in particle size. There are arguments which suggest that the support may be of minimal importance as long as the particles themselves have certain qualities, in particular, a high concentration of low coordinated surface sites [45]. The density of these sites increases with decreasing particle size, and therefore, we do not expect the density of such sites in the Pt/SiO₂ and Pt/CeO₂ samples to be high as compared to the other samples. With the addition of Pt, the previously inert SiO₂ displays a dramatic increase in catalytic activity. Furthermore, the CeO₂ support alone (without Pt) outperforms the Pt/SiO₂ sample (Figs. 5 and 6) and the addition of Pt to the CeO₂ support is expected to enhance its performance even further. Although this was indeed observed, the increase in activity was not as significant as in some of the other catalysts investigated, such as Pt/ZrO₂. It has been reported that the Pt in Pt/CeO₂ is the main catalytic species for the decomposition of MeOH [46]. This suggests that the relatively small improvement observed in this sample can be attributed either to the large size of the Pt particles considered, or perhaps a partial encapsulation of

the Pt particles by CeO₂, also suggested in Ref. [46]. As previously discussed, the possibility of alloy formation in the Pt/CeO₂ samples might also give rise to detrimental effects in the reactivity of this system. Due to the large nanoparticle sizes available in the Pt/CeO₂ and Pt/SiO₂ samples, we will exclude these samples from the comparative discussion of the support effects.

The remaining samples (Pt/ZrO₂, Pt/Al₂O₃, and Pt/TiO₂) all have similar size distributions of ~ 8-9 nm. For these three samples the Pt/ZrO₂ is clearly the most active for the decomposition of MeOH and a support-dependence for this reaction might be inferred. It is interesting to note that the Pt/ZrO₂ and Pt/Al₂O₃ are more active than the Pt/TiO₂, suggesting that irreducible supports may be of advantage for this reaction. In a study done by Ivanov et al. [25] on the electronic state of Pt supported on different oxides, using diffuse reflectance IRS and CO as a probe molecule, it was found that Pt/ZrO₂ revealed absorption bands characteristic of CO complexes with Lewis acid sites on the surface of ZrO₂. In the same study no such features were observed for Pt/TiO₂, Pt/Al₂O₃, or Pt/SiO₂. It has also been found, in a study of MeOH adsorption and dissociation over SnO₂, that the dissociation of MeOH to methoxide occurs preferentially at Sn²⁺ cationic sites. Therefore, acidic sites on the surface of the Pt/ZrO₂ sample may account for its superior performance relative to the other samples.

Conclusion

We have investigated the decomposition of MeOH over Pt deposited on various oxide supports. The samples obtained may be roughly grouped into categories consisting of large (~ 15-18 nm) and small (~ 8-9 nm) Pt particles deposited on *reducible* (CeO₂, TiO₂) and *non-reducible* (SiO₂, ZrO₂, Al₂O₃) supports. For all Pt/oxide samples tested the reaction proceeds mainly through the direct decomposition of MeOH. For the large

particles deposited on highly reducible CeO₂, as well as non-reducible SiO₂, the Pt/CeO₂ is clearly more active. For these two samples, the superior performance of the Pt/CeO₂ sample can be related to the relative performances of the Pt-free supports themselves. However, for the smaller particles, deposited on TiO₂, ZrO₂, and Al₂O₃, the Pt/ZrO₂ is the most active, much more so than the Pt/TiO₂ which reaches 50% conversion at ~ 230°C as compared to ~ 195°C for the Pt/ZrO₂. The Pt/ZrO₂ is also cationic as opposed to the mainly metallic Pt on TiO₂ and Al₂O₃. Further, our XPS data indicate that for similarly sized particles the state of oxidation of Pt depends on the support. Because all samples underwent identical thermal treatments, we may conclude that the stability of Pt^{δ+} species can be affected by the choice of support. These data suggest that for MeOH decomposition, or perhaps in general, for reactions not involving the dissociation of O₂, the reducibility of the support plays a secondary role to the more important parameters of particle size and oxidation state of Pt. The role of the support is that of a stabilizer, a provider of preferential/additional sites of interaction, and a mediator among the different oxides of Pt.

Acknowledgments

We gratefully acknowledge the support of this work by the Donors of the American Chemical Society Petroleum Research Fund under Grant PRF-42701-G5 and supplement for minority undergraduate summer research, and the National Science Foundation (NSF-CAREER award, No. 0448491).

References

- [1] J. Tabatabaei, B.H. Sakakini and K.C. Waugh, *Catal. Lett.* 110 (2006) 77.
- [2] G.A. Olah, *Catal. Lett.* 93 (2004) 1.
- [3] M.S. Spencer, *Topics in Catalysis* 22 (2003) 135.
- [4] T. Shishido, H. Sameshima, K. Takehira, *Topics in Catal.* 22 (2003) 261.
- [5] M. ZumMallen and L.D. Schmidt, *J. Catalysis* 161 (1996) 230.
- [6] C. Panja, N. Saliba and B.E. Koel, *Surf. Sci.* 395 (1998) 248.
- [7] Y. Yang and L. McElwee-White, *Dalton Trans.* (2004) 2352.
- [8] D. Cao, G.Q. Lu, A. Wieckowski, S. A. Wasileski and M. Neurock, *J. Phys. Chem. B.* 109, (2005) 11622.
- [9] Y. Y. Tong, H. S. Kim, P. K. Babu, P. Wazczuk, A. Wiekowski and E. Oldfield, *J. Am. Chem. Soc.* 124, (2002) 468.
- [10] P.J. Ferreira, G.J. la O', Y. Shao-Horn, D. Morgan, R. Makharia, S. Kocha and H.A. Gasteiger, *J. Electrochem. Soc.* 152, A2256 (2005)].
- [11] B. L. M. Hendriksen and J. W. M. Frenken, *Phys. Rev. Lett.* 89, (2002) 046101.
- [12] V.A.T. Dam and F.A. de Bruijn, *J. Electrochem. Soc.* 154 (2007). B494.
- [13] R. Hull, L. Li, Y. Xing and C. C. Chusuei, *Chem. Mater.* 18 (2006) 1780.
- [14] H. A. Gasteiger, S. S. Kocha, B. Sompalli and F. T. Wagner, *Appl. Catal. Environ. B* 56 (2005) 9.
- [15] J. Croy, S. Mostafa, J. Liu, Y. Sohn and B. Roldan Cuenya, *Catal. Lett.* (2007), DOI: 10.1007/S10562-007-9162-1, in press.
- [16] M. Haruta, *CATTECH* 6 (2002) 102.
- [17] Y. Men, H. Gnaser, R. Zapf, V. Hessel and C. Ziegler, *Catal. Comm.* 5 (2004) 671.
- [18] M. Kurtz, J. Strunk, O. Hinrichsen, M. Muhler, K. Fink, B. Meyer and Ch. Wöll, *Angew. Chem. Int.* 44 (2005) 2790.
- [19] T. Dellwig, J. Hartmann, J. Libuda, I. Meusel, G. Rupprechter, H. Unterhalt and H.J. Freund, *J. Mol. Catal. A* 162 (2000) 51.
- [20] C. Hardacre, R.M. Ormerod and R.M. Lambert, *J. Phys. Chem.* 98 (1994) 10901.
- [21] A. Badri, C. Binet and J.C. Lavalley, *J. Chem. Soc. Faraday Trans.* 92 (1996) 1603.
- [22] B.R. Powell and S.E. Whittington, *J. Catal.* 81 (1983) 382.
- [23] H.P. Sun, X.P. Pan, G.W. Graham, H.W. Jen, R.W. McCabe, S. Thevuthasan and C.H.F. Peden, *Appl. Phys. Lett.* 87 (2005) 201915.

- [24] O. Dulub, W. Hebenstreit and U. Diebold, *Phys. Rev. Lett.* 84 (2000) 3646.
- [25] A.V. Ivanov and L.M. Kustov, *Russ. Chem. Bull.* 47 (1998) 1061.
- [26] J.P. Spatz, S. Mossmer, C. Hartmann, M. Moller, T. Herzog, M. Krieger, H.G. Boyen, P. Ziemann and B. Kabius, *Langmuir* 16 (2000) 407.
- [27] B. Roldan Cuenya, S.H. Baeck, T.F. Jaramillo and E.W. McFarland, *J. Am. Chem. Soc.* 125 (2003) 12929.
- [28] L.K. Ono, D. Sudfeld and B. Roldan Cuenya, *Surf. Sci.* 600 (2006) 5041.
- [29] G.C. Bond and S. Flamerz, *Appl. Catal.* 46 (1989) 89.
- [30] Y. Sena, G. Dogu and T. Dogu, *Catal. Today* 117 (2006) 271
- [31] G. Corro, J.L.G. Fierro and V.C. Odilon, *Catal. Commun.* 4 (2003) 371.
- [32] M.L. Miller and R.W. Linton, *Anal. Chem.* 57 (1985) 2314.
- [33] A.E. Hughes and B.A. Sexton, *J. Electron Spectrosc.* 50 (1990) 15.
- [34] S.A. Lee, K.W. Park, J.H. Choi, B.K. Kwon and Y.E. Sung, *J. Electrochem. Soc.* 149 (2002) 1299.
- [35] V. Perrichon, L. Retailleau, P. Bazin, M. Daturi and J.C. Lavalley, *Appl. Catal. A* 260 (2004) 1.
- [36] S. Penner, D. Wang, R. Podloucky, R. Schlogl and K. Hayek, *Phys. Chem. Chem. Phys.* 6 (2004) 5244.
- [37] J. Tang, J.M. Lawrence and J.C. Hemminger
- [38] M. Chen and L.D. Schmidt, *J. Catal.* 55 (1978) 348.
- [39] J. Silvestre-Albero, A. Sepulveda-Escribano, F. Rodriguez-Reinoso and J.A. Anderson, *J. Catal.* 223 (2004) 179.
- [40] S. Laursen and S. Linic, *Phys. Rev. Lett.* 97 (2006) 026101.
- [41] O. Bjorneholm, F. Federmann, F. Fossing and T. Moller, *Phys. Rev. Lett.* 74 (1995) 3017.
- [42] Q. Fu, H. Saltsburg and M. Flytzani-Stephanopoulos, *Science* 301 (2003) 935.
- [43] Y. Matsumura, M. Okumura, Y. Usami, K. Kagawa, H. Yamashita, M. Anpo and M. Haruta, *Catal. Lett.* 44 (1997) 189.
- [44] Y. Usami, K. Kagawa, M. Kawazoe, Y. Matsumura, H. Sakurai and M. Haruta, *Appl. Catal. A* 171 (1998) 123.
- [45] N. Lopez, T.V.W. Janssens, B.S. Clausen, Y. Xu, M. Mavrikakis, T. Bligaard and J.K. Norskov, *J. Catal.* 223 (2004) 232.
- [46] S. Imamura, T. Hagashihara, Y. Saito, H. Aritani, H. Kanai, Y. Matsumura and N. Tsuda, *Catal. Today* 50 (1999) 369.

Figure captions:

Figure 1. Tapping mode AFM images of size-selected Pt nanoparticles dip-coated on $\text{SiO}_2/\text{Si}(001)$ and annealed in UHV at 500°C for 30 min. Samples were prepared using Pt/PVP concentrations of 0.6 (a) and 0.2 (b). The z scale is 0-20nm for (a) and 0-10nm for (b).

Figure 2. Pt nanoparticles prepared by micelle encapsulation supported on CeO_2 : (a) high angle annular dark field image obtained by scanning transmission electron microscopy (STEM) of Pt/ CeO_2 (#1), (b) bright field image of same region as in (a), (c) high magnification image of Pt particle indicated by the circles in (a) and (b) and marked with a (1), (d) Pt particle on CeO_2 from Pt/ CeO_2 (#2) prepared initially with a solution of smaller Pt particles [fig 1 (b)]. Both samples were annealed at 500°C .

Figure 3. Pt nanoparticles prepared by micelle encapsulation supported on selected oxide powders: (a) Pt/ SiO_2 , (b) Pt/ Al_2O_3 , (c)-(d) Pt/ ZrO_2 . All samples were annealed at 500°C .

Figure 4. (a) Pt-4f core level XPS spectra of Pt nanoparticles supported on: (from top to bottom) TiO_2 , ZrO_2 , SiO_2 , CeO_2 (#1). (b) Pt $4d_{5/2}$ from Pt/ Al_2O_3 . (c) Al $2p_{3/2}$ before and after the addition of Pt. All spectra were measured after removal of the encapsulating polymer by annealing in air at 500°C .

Figure 5. Catalytic activity (conversion) and selectivity of commercial nanocrystalline oxide powders for MeOH decomposition with average grain sizes of ~ 32 nm for TiO₂ (a), ~ 40 nm for CeO₂ (b), ~ 45 nm for ZrO₂ (c), and ~ 35 nm for Al₂O₃ (d). The number across the top of each chart gives the MeOH conversion (%) at each temperature. SiO₂ (not shown) is almost completely inert, showing only ~ 3% MeOH conversion at 300°C. All powders have been calcined at 500°C for 2.5 hours before the reaction.

Figure 6. MeOH decomposition over Pt nanoparticles supported on nanocrystalline oxide powders: Pt/ZrO₂ (full circles), Pt/Al₂O₃ (full triangles), Pt/TiO₂ (full squares), Pt/CeO₂(#1) (full diamonds), Pt/CeO₂(#2) (open diamonds), Pt/SiO₂ (crosses). All samples have been calcined at 500°C for 2.5 hours before the reaction.

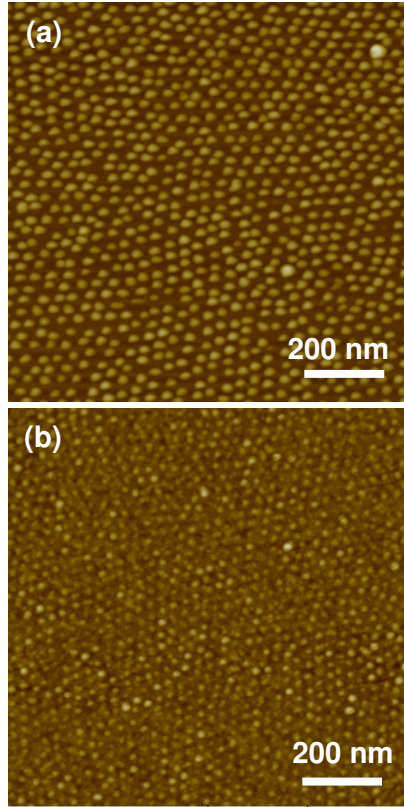


Fig. 1, Croy et al.

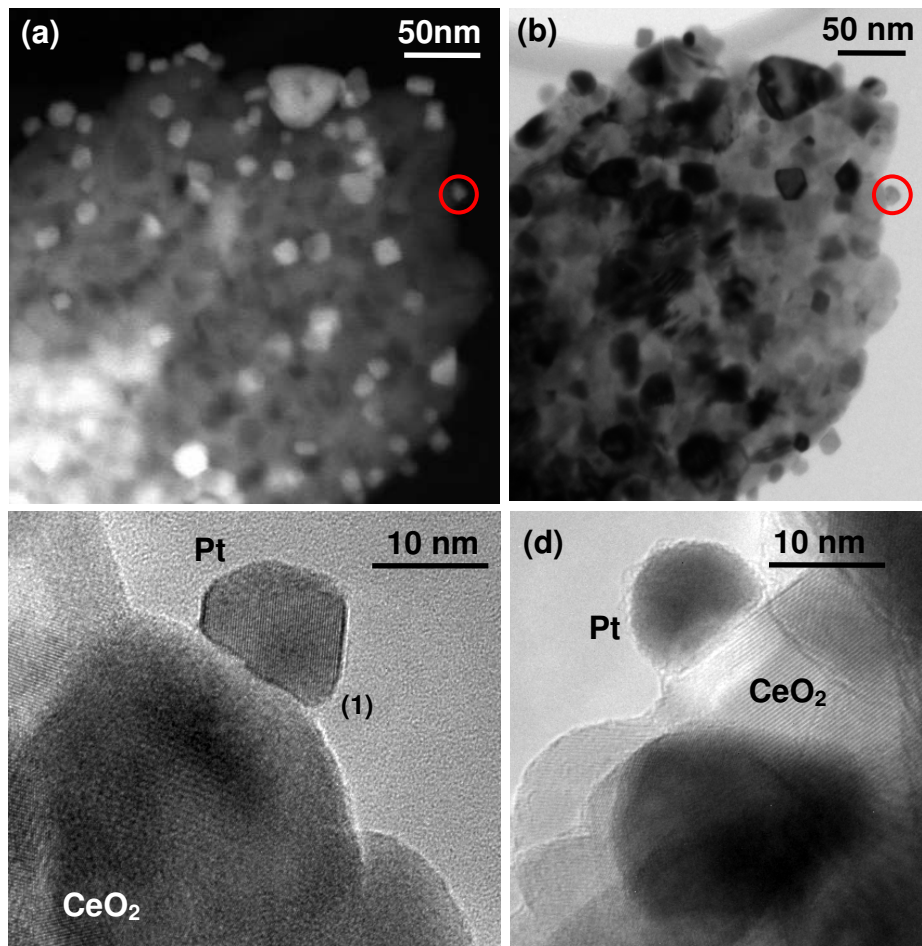


Fig. 2, Croy et al.

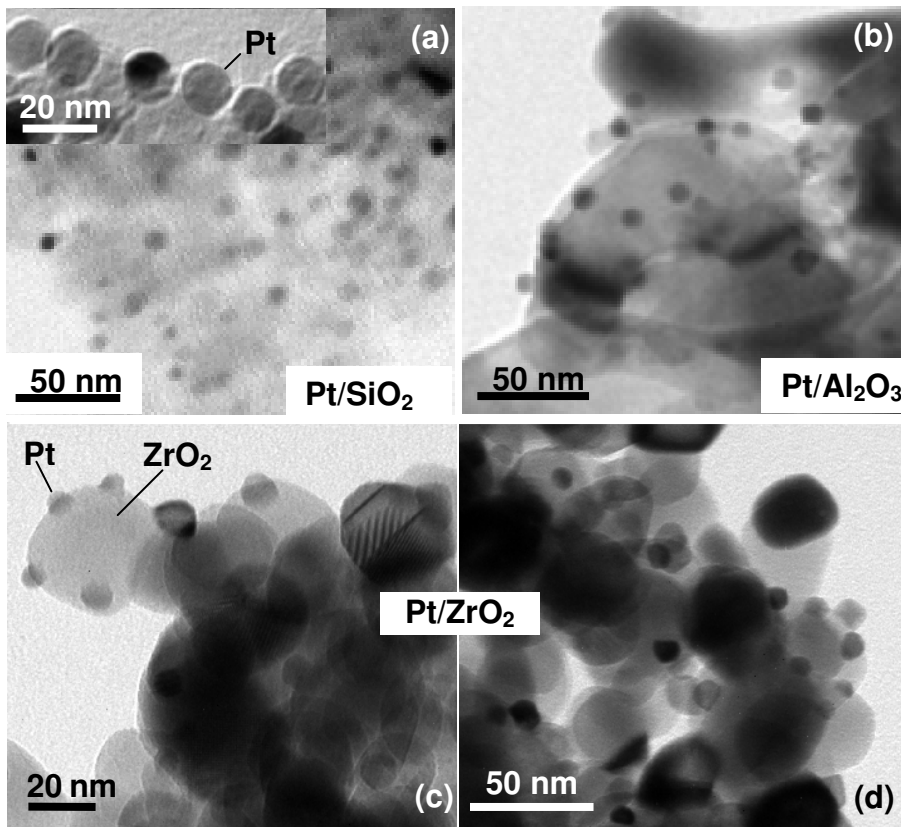


Fig. 3, Croy et al.

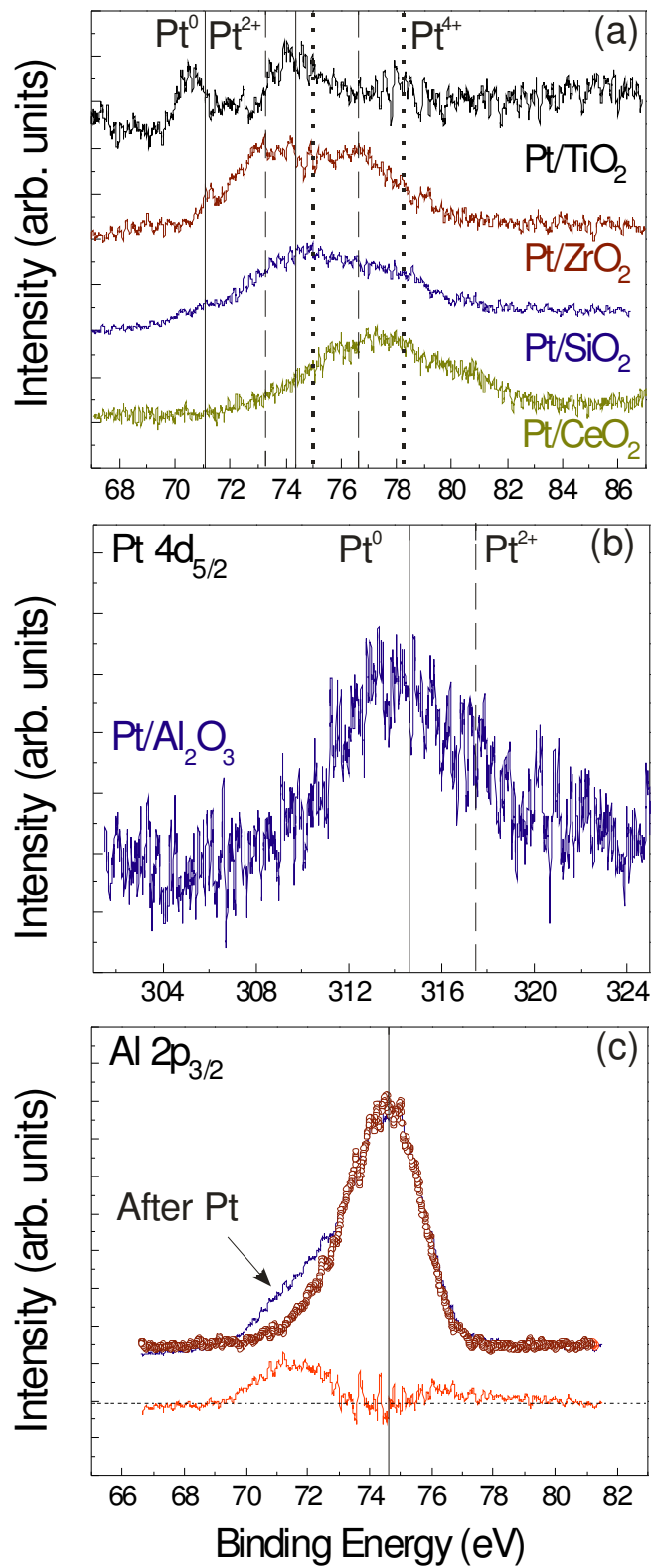


Fig. 4, Croy et al.

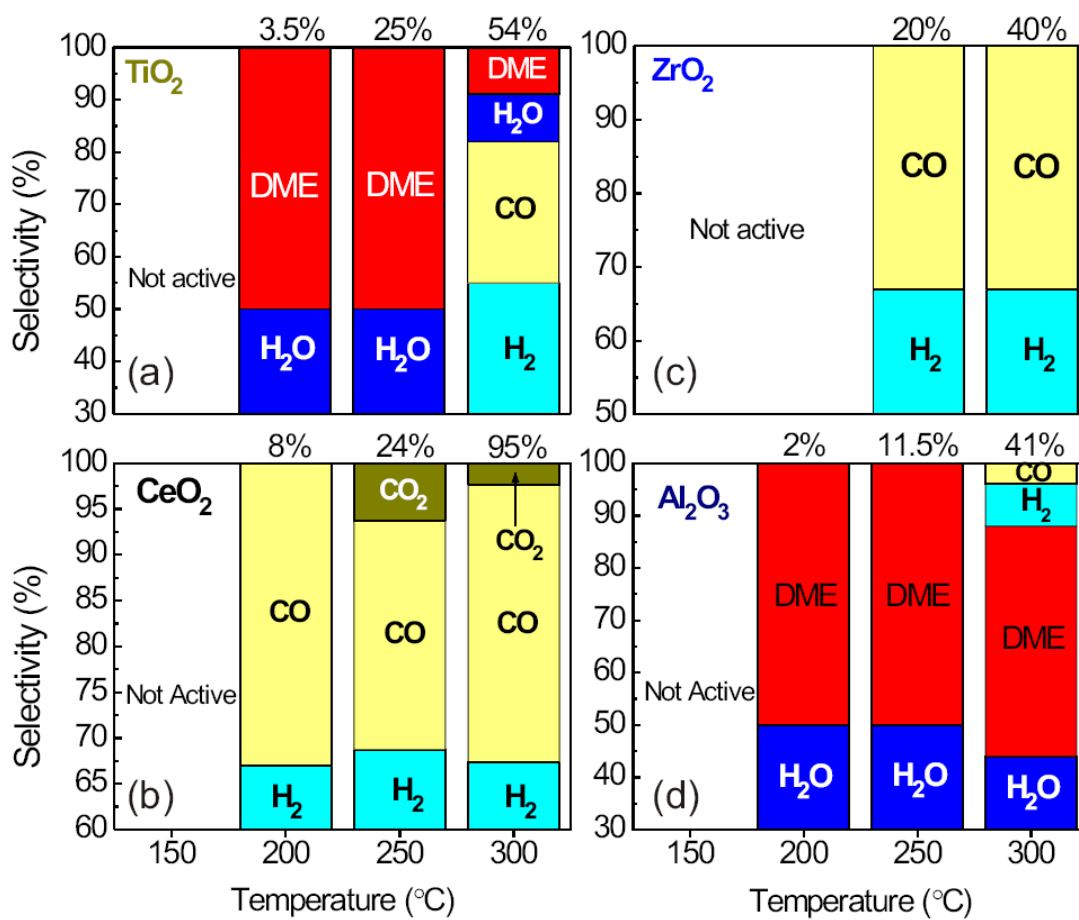


Fig. 5, Croy et al.

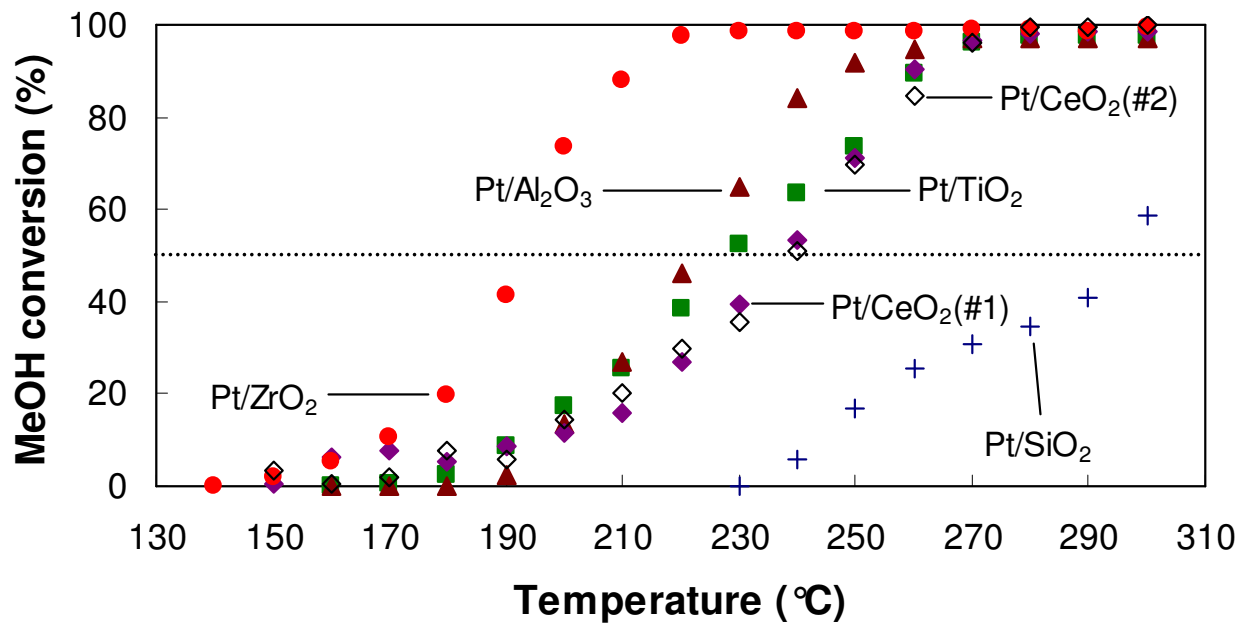


Fig. 6, Croy et al.